ACS NANO

www.acsnano.org

ARTICLE

$[Ag_{62}S_{12}(CBT)_{32}]^{4+}$: A 2.2 nm Two-Electron Superatomic Carborane-Thiolated Silver Nanocluster Exhibiting Multilayer Charge Separation

Arijit Jana, Vivek Yadav, Monika Kučeráková, Sami Malola, Amoghavarsha Ramachandra Kini, Swetashree Acharya, Ajay K. Poonia, Jan Macháček, Kumaran Nair Valsala Devi Adarsh,* Hannu Häkkinen,* Tomas Base,* and Thalappil Pradeep*

Cite This: https://doi.org/10.1021/acsnano.5c11836

ABSTRACT: Investigating large metal nanoclusters decorated with three-dimensional molecular cages, with complete structural characterization, is challenging; however, their detailed understanding is important to study electronic confinement and associated properties. We have structurally resolved a nearly spherical 2.2 nm silver cluster with the molecular composition $[Ag_{62}S_{12}(CBT)_{32}]^{4+}$, altogether having 842 atoms, solely protected with *meta*-carborane-thiolates (CBTs). This is the largest nanocluster with carborane-based molecular cages reported so far. Abscission of the cluster reveals that it has a face-centered-cubic Ag_{14} inner core encapsulated with 12 sulfides, which is further surrounded by an outer scaffold of $Ag_{48}-S_{32}$ shell, protected with 32 *meta*-carboranes. The silver-sulfide skeleton of the nanocluster showed an assembly of multilayered polyhedra, having a mixture of Platonic and Archimedean solids. High-resolution mass spectrometric analyses and other spectroscopic studies further confirmed the molecular composition. This nanocluster exhibits characteristic molecular multiband optical absorption features along with a weak near-infrared (NIR) emission band. Ultrafast femtosecond transient absorption studies revealed stable photoexcited states linked to interlayer electron mobility between the neutral Ag_{14} core and the positively charged Ag_{48} shell, which are surrounded by negatively charged sulfide (S_{12} and S_{32}) layers. Computational analysis shows that this cluster behaves as a two-electron superatom with a band gap of 1.77 eV, which is associated with the energy difference between the 1S symmetric and 1P nonsymmetric states. Successful structural characterization and associated optical properties of the nanocluster suggested that other larger metal nanoclusters encapsulated by three-dimensional molecular cages may be suitable for single-particle photonic and optoelectronic applications.

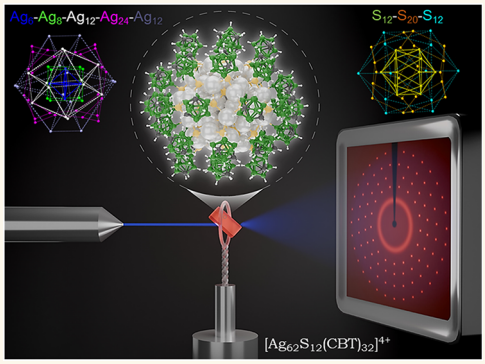

KEYWORDS: *silver nanoclusters, carboranes, polyhedral nests, superatoms, optical properties, multilayer charge separation*

INTRODUCTION

Monolayer-protected metal clusters or nanoclusters of 1 to 3 nm core diameter have emerged as an interesting class of precise nanomaterials bridging the gap between single atoms (as in the form of molecular complexes) and traditional nanoparticles.[1−3] These nanoscale objects exhibit molecule-like discrete energy levels leading to characteristic optical and electrochemical properties.[4,5] Specific electronic structure with transitions within these confined energy levels also results in phenomena such as electrochemiluminescence,[6] photoluminescence,[7] and size-dependent electronic conductivity.[8] They have diverse uses in fields such as solar cells,[9] biomedicine,[10] sensing,[11,12] radiosensitization,[13] catalysis,[14,15] laser printing,[16] and photothermal applications.[17,18] Among the various metal clusters, those composed of noble metals, such as gold, silver, and copper, are particularly prominent due to their ease of

Received: July 15, 2025
Revised: September 16, 2025
Accepted: September 18, 2025

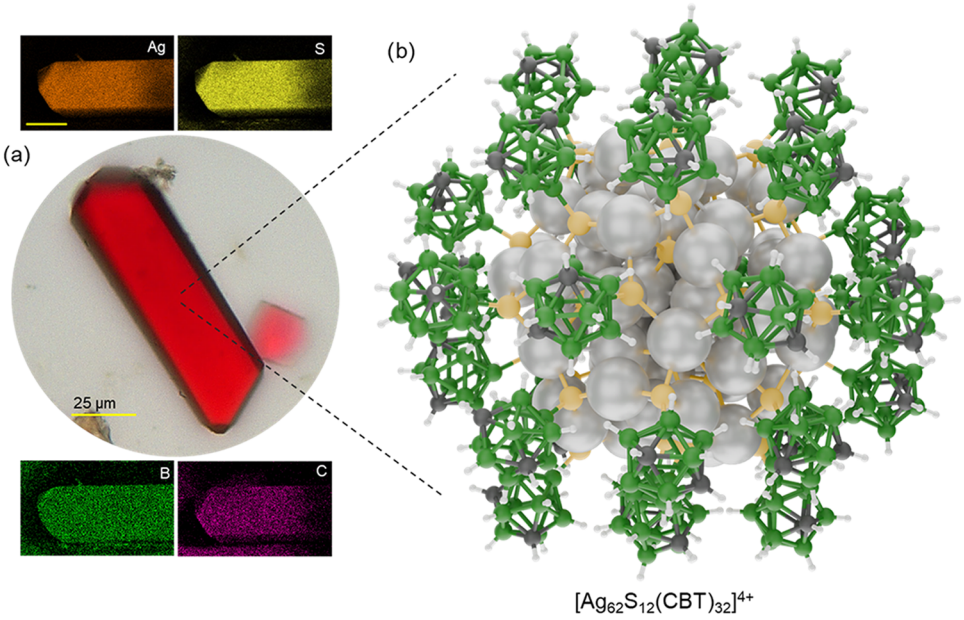

Figure 1. (a) Optical micrograph of a cuboidal single crystal of the $[Ag_{62}S_{12}(CBT)_{32}]^{4+}$ nanocluster. The inset shows the EDS elemental mapping of the crystal, having the elements Ag, S, B, and C in it (scale bar 25 μm). (b) Complete molecular structure of the $[Ag_{62}S_{12}(CBT)_{32}]^{4+}$ cluster. Color codes: metallic gray = silver, yellow = sulfur, green = boron, gray = carbon, and white = hydrogen.

synthesis, stability, structural characteristics, and drastic changes induced by atomic-level modifications.[1−3] Sometimes, in addition to structures consisting of metal cores and thiolate-anchored outer ligands, the clusters exhibit more complicated inner compositions with chalcogen atoms (S, Se, and Te) forming a multilayer structure with metal cores, metal sulfide interlayers, and ligand structures.[19,20] Some of these structurally resolved silver chalcogenide clusters are $[Ag_{14}S(SC_6H_4NCS)_{12}(PPh_3)_8]$,[21] $[Ag_{115}S_{34}(SCH_2C_6H_4{}^tBu)_{47}(dpph)_6]$,[22] $[Ag_{70}S_{20}(SPh)_{28}(dppm)_{10}]$,[23] $[Ag_{262}S_{100}(S^tBu)_{62}(dppb)_6]$,[23] $[Ag_{154}Se_{77}(dppxy)_{18}]$,[24] $[Ag_{320}(S^tBu)_{60}S_{130}(dppp)_{12}]$,[24] $[Ag_{352}S_{128}(S^tC_5H_{11})_{96}]$,[24] and $[Ag_{490}S_{188}(S^tC_5H_{11})_{114}]$.[24] Most of these clusters were synthesized through reduction using silylated metal chalcogenide sources. Embedding chalcogen atoms in the cluster framework, as well as heterometal doping in them, has been reported to enhance structural stability and boost the electron mobility within the framework. As a result, enhanced emission characteristics and efficient photoelectric responses were observed in these nanomaterials.[25,26]

Among the various silver nanoclusters, those of specific dimensions exhibit distinct electronic properties. For example, silver nanoclusters with the nuclearity between 4 and 50 atoms show multiband optical absorption features, while those in the nuclearity range from 51 to 120 exhibit a continuous transition to the plasmonic regime, and nuclearity beyond 150 is plasmonic.[27] Although the second category of materials is interesting for size−property correlations, only a handful of such clusters have been structurally resolved to date. In monolayer-protected silver clusters, organic molecules such as thiols,[28−34] phosphines,[35] alkynes,[36,37] carbenes,[38] dithiophosphates,[39] amides,[40] deoxyribonucleic acids,[41] thiacalixarenes,[42,43] and carboxylates[44] are used as protective ligands, and they play crucial roles in controlling the nuclearity and electronic properties of the clusters. These ligands also bring structural stability to these nanoentities through interfacial charge transfer between the metal core and the ligand shell. Structure-specific properties can also be tuned by chemical modifications of the ligands. Among the various thiols, carborane-thiol cage molecules emerged as an interesting class of ligands with robust thermal and chemical stability and three-dimensional aromaticity dispersed around the icosahedral C_2B_{10} cage.[45−47] In combination, metal nanoclusters protected by carboranethiols have been reported to possess greater stability and chemical functionalities, as well. In addition, they show tunable luminescence,[48,49] catalytic activity,[50,51] sensing capability,[52] nanomechanical properties,[53] and they are also promising as high-energy hypergolic materials.[54,55] Compared to conventional organic thiols, carboranethiols have most often resulted in silver clusters with lower nuclearity, such as $[Ag_{14}(C_2B_{10}H_{10}S_2)_6(CH_3CN)_8]$,[56] $[Ag_{14}(C_2B_{10}H_{10}S_2)_6(C_5H_5N)_8]$,[56] $[Ag_{14}(C_2B_{10}H_{10}S_2)_6(C_6H_7N)_8]$,[56] $[Ag_{14}(C_2B_{10}H_{10}S_2)_6(PPh_3)_6]$,[57] $[Ag_{17}I_3S(C_2B_{10}H_{10}S_2)_6(CH_3CN)_{11}]$,[58] $[Ag_{17}(C_2B_{10}H_{11}S)_{12}]$,[59] $[Ag_{21}(C_2B_{10}H_{11}S)_{12}(PPh_3)_2]$,[60] $[Ag_{30}(C_2B_{10}H_9S_3)_8(C_{25}H_{22}P_2)_6]$,[61] and $[Ag_{33}(C_2B_{10}H_{10}S_2)_{12}]$.[62] The 3D architecture and associated steric demands of the cage ligands make the formation of large metal clusters challenging. In this regard, we report here a breakthrough in the preparation of a large silver/silver chalcogenide cluster, comprising 62 silver atoms, 12 sulfides, and a surface envelope consisting of 32 *meta*-carborane-thiolate ligands, altogether having 842 atoms.

RESULTS AND DISCUSSION

Synthesis and Structural Details. The $[Ag_{62}S_{12}(CBT)_{32}]^{4+}$ (abbreviated as Ag_{62}) nanocluster was synthesized through dimethylformamide/methanol (DMF/MeOH, 2:1 by volume) assisted thermochemical reduction of silver nitrate in the presence of the M_9-COOH precursor (where M_9-COOH is *meta*-carborane-9-thiol-12-carboxylic acid). In brief, solvothermal treatment (75 ± 3 °C for 15 h)

https://doi.org/10.1021/acsnano.5c11836
ACS Nano XXXX, XXX, XXX−XXX

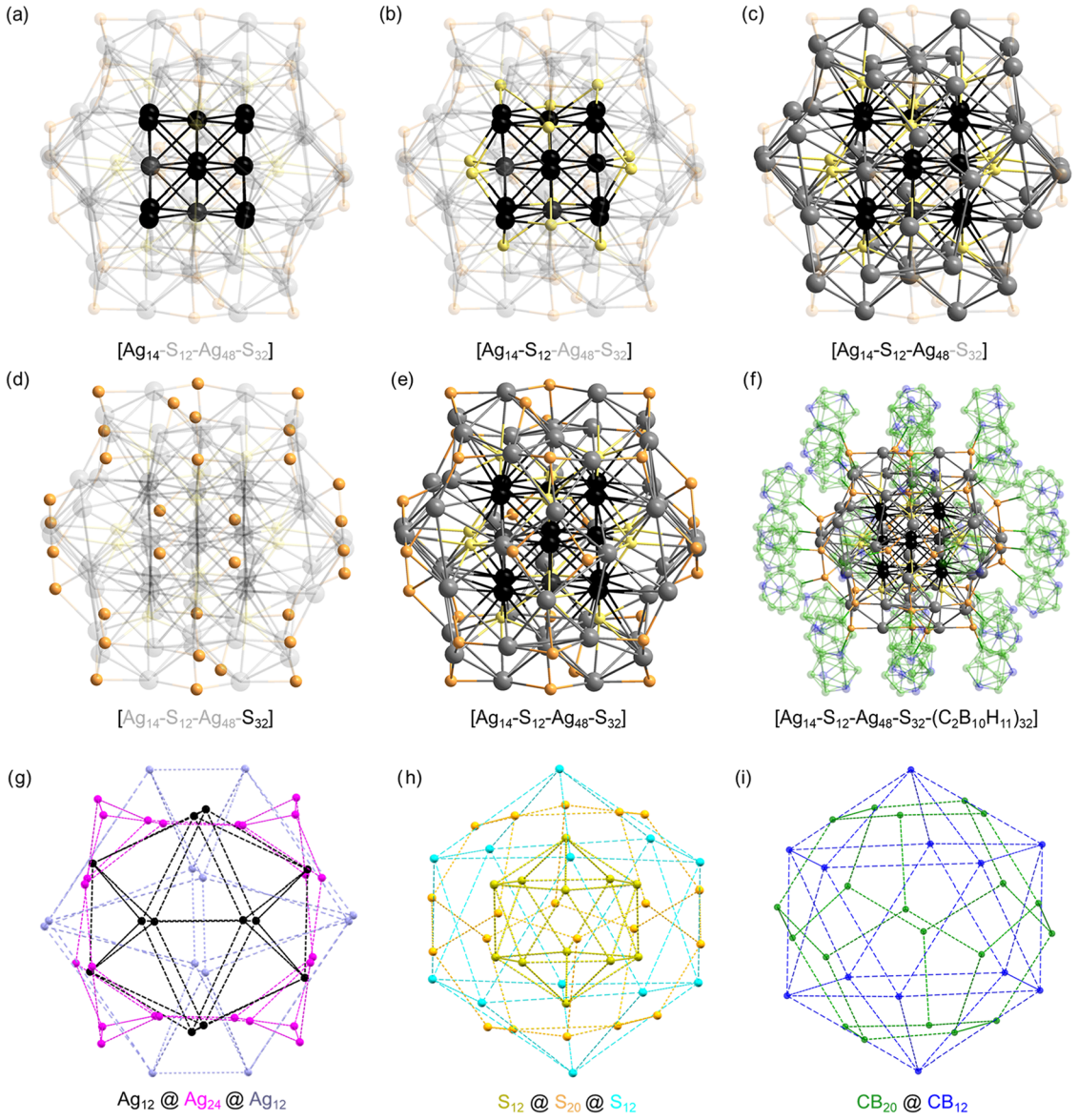

Figure 2. Structural anatomy of the $[Ag_{62}S_{12}(CBT)_{32}]^{4+}$ cluster. (a) The innermost Ag_6 octahedron, surrounded by eight capping Ag atoms, resulted in an Ag_{14} geometry. (b) Ag_{14} is surrounded by 12 interstitial sulfides, resulting in the Ag_{14}–S_{12} structure. (c) Ag_{14}–S_{12} is further protected by the Ag_{48} shell. (d) Arrangement of the 32 sulfur atoms connected with the carboranes. (e) The total silver-sulfide skeleton of the cluster. (f) Complete structural skeleton of the cluster along with carborane ligands. Hydrogen atoms are removed for clarity. Color code: black and gray = silver, yellow and orange = sulfur, green = boron, and blue = carbon. Alignment of multilayer symmetry element in the structural skeleton outside the fcc-Ag_{14}: (g) the outer Ag_{48} shell can be viewed as an icosahedron (Ag_{12}), a truncated cube (Ag_{24}), and a distorted icosahedron (Ag_{12}). (h) The 12 interstitial sulfides and outer 32 thiolate sulfur atoms can be viewed as an inner icosahedron (S_{12}), dodecahedron (S_{20}), and outer icosahedron (S_{12}). (i) The centroids of 32 carboranes can be visualized as an interpenetration dodecahedron (CB_{20}) and an icosahedron (CB_{12}).

of an equimolar mixture of $AgNO_3$ and M_9-COOH in DMF/MeOH placed in a hydrothermal bomb or closed glass container resulted in the red-colored Ag_{62} cluster. Time-dependent growth of the cluster, monitored by UV–vis absorption spectroscopy, is shown in Figure S1 (more synthetic details are provided in the Experimental Section). To understand the specific role of the M_9-COOH ligand, a similar solvothermal synthesis was performed using the *meta*-carborane 9-thiol (M_9) ligand. However, this reaction did not result in any distinct features of Ag_{62} clusters (shown in Figure S2). It may be noted that we have synthesized and purified the M_9-COOH ligand according to our earlier report.[63] To further assess the purity of the compound, we conducted mass spectrometry, Infrared (IR) spectroscopy, and Raman analysis (see Figures S3 and S4). These investigations confirm the presence of the −COOH group attached to the carborane cage. Most of the silver clusters have been synthesized either from silver-thiolate precursors using chemical reducing agents like sodium borohydride, sodium cyanoborohydride, or borane-amine complexes, or through ligand exchange reactions starting from pre-existing clusters under either low-temperature or ambient conditions.[64−66] However, the formation of the Ag_{62} cluster using thermal decarboxylation of Ag-M_9-COOH thiolates reported here differs from the usual methods. To investigate the decarboxylation of the M_9-COOH ligand during thermal treatment, we conducted a comparative

https://doi.org/10.1021/acsnano.5c11836
ACS Nano XXXX, XXX, XXX−XXX

$^{11}B\{^{1}H\}$ NMR analysis of the M_9-COOH ligand before and after thermal treatment at 55 °C. The NMR spectra (shown in Figure S5) clearly demonstrate the decarboxylation of the M_9-COOH ligand that occurred during thermal treatment. We have also tried the direct reduction of $AgNO_3$ and M_9 precursors using $NaBH_4$ and $NaBH_3CN$ as reducing agents (shown in Figures S6 and S7). However, these methods did not result in the desired Ag_{62} cluster.

It shows the synthesis without any of the conventional reducing agents and occurs at a relatively higher temperature. Despite numerous challenges in crystallization, single crystals were successfully grown with a yield of ∼75% from the saturated solution of the cluster in the DMF/MeOH (1:1, by volume) mixture. An optical micrograph of a typical red-colored single crystal is shown in Figure 1a. The inset of Figure S1 shows many such crystals. Energy-dispersive spectroscopy (EDS) elemental mapping of different single crystals revealed the presence of the respective elements, as shown in the inset of Figure 1a. The atomic percentages of silver, sulfur, and the combined elements of boron and carbon in the crystal are approximately 8.60%, 6.49%, and 55.37%, respectively, which closely align with the nominal stoichiometry of the cluster. Additionally, nitrogen and oxygen, associated with the nitrate (NO_3^-) counterions, are also detected in the crystal (shown in Figure S8).

Single-crystal X-ray diffraction showed that the cluster crystallizes in a monoclinic crystal system with the space group $P2_1/n$ (additional crystallographic details are summarized in Table S1). The complete molecular structure of the cluster consists of 62 silver atoms, 12 sulfides, and 32 *meta*-carborane-thiolates filling up the surface (shown in Figure 1b). The inner sulfur atoms in the structure of $[Ag_{62}S_{12}(CBT)_{32}]^{4+}$ come from M_9-COOH itself, as no other sulfur source was used in the synthesis. Similar thiol dissociative processes giving sulfur are known in the cluster literature.[20] Complete set of crystallographic data, including structural refinement, is in the Supporting Information. Detailed analysis of the silver/silver-sulfide skeleton of the cluster can be visualized as an $Ag_{14}-S_{12}$ inner core encapsulated by a shell of $Ag_{48}-S_{32}$. Formation of the molecular skeleton of the cluster (shown in Figure 2a–2f) starts with a face-centered cubic (fcc) Ag_{14} inner core, in which the average Ag–Ag distance of 2.87 Å indicates a strong Ag–Ag interaction as in bulk silver (see Figure 2a). This Ag_{14} core can be described as an Ag_6 octahedron surrounded by eight Ag atoms in a cubic fashion, forming Ag_6-Ag_8 geometry. The Ag_{14} core is further enclosed by 12 sulfides, each exhibiting triple coordination (μ_3) with the Ag_{14} framework, and Ag–S bond distance ranging between 2.49 and 2.63 Å (see Figures 2b and S3). More precisely, two of the Ag–S bonds are connected to the outer Ag_8 cube, while the third Ag–S bond is connected to the inner Ag_6 octahedron (see Figure S9). Structural expansion of the framework upon considering the $Ag_{14}-S_{12}$ core and the $Ag_{48}-S_{32}$ shell revealed that among the 12 inner sulfides, two exhibit μ_7 coordination, two adopt μ_8 coordination, and the remaining eight display μ_6 coordination with Ag atoms (see Figure S10).

The outer framework beyond the $Ag_{14}-S_{12}$ of the cluster comprises an encapsulating $Ag_{48}-S_{32}$ silver-sulfide shell (shown in Figure 2c,d). The complete silver-sulfide skeleton is further surrounded by 32 *meta*-carboranes (Figure 2e,2f). Structural analysis of the $Ag_{48}-S_{32}$ shell reveals an $Ag_{32}S_{12}$ ring, further enclosed by subunits of three distinct types: Ag_2S_4, Ag_2S_4, and Ag_4S_2 (see Figure S11). Two units of each subunit type are arranged in opposite positions of the $Ag_{32}S_{12}$ envelope. Each of these outer Ag atoms forms μ_3, μ_4, and μ_5 intermetallic coordination with an Ag–Ag distance of 3.02 to 3.81 Å (shown in Figures S11 and S12).

Symmetry Analysis and Solid-State Packing. We conducted an analysis of the symmetry elements present in the multilayer skeleton of the cluster. The inner skeleton of the cluster is composed of fcc Ag_{14} (Figure 2a), and the outer Ag_{48} skeleton is composed of three layers. The innermost layer of 12 Ag atoms forms a regular icosahedron (Ih) with Ag_{12} (Schläfli symbol (3,5)). The next layer is formed by an Archimedean solid, which is a truncated cube with Ag_{24} units (Schläfli symbol t{4,3}). This is followed by a distorted Ag_{12} icosahedron (Schläfli symbol (3,5)). Notably, each of the two corners of the inner and outer icosahedra is cross-linked with each of the octagonal faces of the truncated cube (see Figures 2g and S13). Next, we analyzed the sulfur atoms, which include 12 inner sulfides and 32 outer thiolated S atoms. The sulfides form an inner S_{12} icosahedron (Ih) (Schläfli symbol (3,5)), and the outer 32 thiolated S atoms create an S_{20} dodecahedron (Ih) (Schläfli symbol (5,3)). This is followed by another S_{12} icosahedron (Ih) (Schläfli symbol (3,5)), which is larger in size (see Figures 2h and S14). These two icosahedra are stacked on top of each other, with the corners of each one pointing toward the centroid of each pentagonal face of the S_{20} dodecahedron.

More careful analysis reveals that all of the carborane cages are arranged in two ways, where the first group of ligands was surrounded by five nearby carboranes and the other category of carboranes was surrounded by six carboranes. We have observed that out of 32 carboranes, 12 result in pentagonal surface cavities, while 20 exhibit hexagonal surface cavities (see Figure S15). A more detailed analysis of the symmetry arrangement of all of the carborane centroids shows that they form an interpenetrating CB_{20} dodecahedron (Ih), as well as a CB_{12} icosahedron (Ih), which correlates with hexagonal and pentagonal surface envelopes (see Figures 2i and S16). All of the carborane-thiolate ligands adopt μ_3-coordination modes with Ag–S distances within the range of 2.39–3.00 Å (see Figure S17). Due to the structural complexity, some disorder has been observed in the outer sulfur atoms (as depicted in Figure S18). The unit cell packing comprises six clusters, with four molecules aligned along the center of the *b*-axis and two positioned along the center of the *ac* plane, resulting in an overall packing density (Z) of 2 (see Figure S19).

The three-dimensional extended supramolecular packing of the cluster molecules reveals lamellar packing of clusters (see Figure S20), which enables intermolecular B–H···B, B–H···H–C, B···H–C, and C–H···B interactions between the clusters via their carborane ligands (see Figure S21). These interactions are prominent between the large clusters, as each cluster molecule features 32 carborane molecules on its surface. The electrostatic potential map of a *meta*-carborane-9-thiol molecule exhibits dipole–dipole and electrostatic interactions between C–H and H–B of carboranes that constitute the surface shell in the Ag_{62} cluster, which is also correlated with our previously reported studies (see Figure S22).[63,67,68] Residual electron density maps were observed in the extended lattice, attributed to the presence of solvent molecules and counterions (see Figure S23). We note that this is the largest atomically precise metal cluster reported to date, featuring carborane-based ligands on its surface. Table S2 presents a detailed summary of all of the structurally resolved carborane-

https://doi.org/10.1021/acsnano.5c11836
ACS Nano XXXX, XXX, XXX–XXX

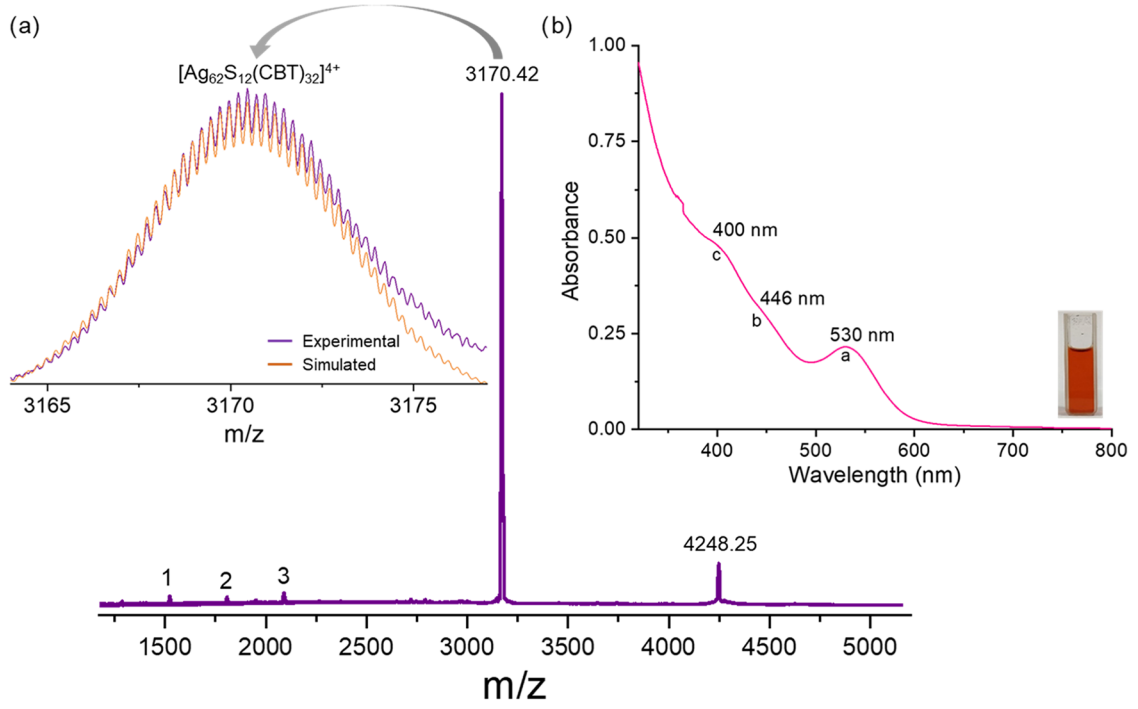

Figure 3. (a) Positive-ion mode ESI-MS spectrum of the cluster. The prominent peak at m/z 3170.42 with a charge state of 4+ confirmed the composition as $[Ag_{62}S_{12}(CBT)_{32}]^{4+}$. Another minor peak at m/z 4248.25 (charge state of 3+) is assigned as the $[Ag_{62}S_{12}(CBT)_{32}\cdot(MeO)\cdot(MeOH)]^{3+}$ species. Other peaks marked as 1 (m/z 1523.60), 2 (m/z 1806.60), and 3 (m/z 2089.61) are assigned to the formation of species $[Ag_6(CBT)_5]^+$, $[Ag_7(CBT)_6]^+$, and $[Ag_8(CBT)_7]^+$, respectively. The left inset shows an exact matching of the isotopic distributions of the high-resolution experimental spectrum with the simulated one, with a spacing of m/z 0.25. (b) UV−vis absorption spectrum of the Ag_{62} cluster in DMF, with peaks marked. The inset shows a photograph of the cluster solution in DMF.

thiolated and carborane-alkynylated metal clusters reported so far.

Mass Spectrometry and Spectroscopic Characterization. High-resolution mass spectrometry (instrumentation and sample preparation provided in the Supporting Information) was performed to further investigate the molecular cluster, gain additional independent insights into its composition, and examine its ionic character. The positive-ion mode electrospray ionization (ESI) mass spectrum shows a prominent peak at m/z = 3170.42 (Figure 3a). The m/z difference between two successive peaks is 0.25, indicating that the cluster carries a charge of 4+. Thus, the total molecular mass of 12681.68 is assigned to the composition $[Ag_{62}S_{12}(CBT)_{32}]^{4+}$ with the experimental isotopic distribution pattern (purple trace) matching well with the simulated one (orange trace) (inset of Figure 3a). Another minor peak at m/z 4248.25 shows the 3+ charge state assigned with the composition $[Ag_{62}S_{12}(CBT)_{32}\cdot(MeO)\cdot(MeOH)]^{3+}$, and it indicates solvation of the parent cluster with methanol and methoxide. Collision energy (CE)-dependent MS-MS fragmentation analysis was performed on the m/z 3170.42 peak (shown in Figure S24).

Upon sequential increase of the CE from 0 to 40 eV, a prominent peak corresponding to m/z 3126.58 with a 4+ charge state was formed because of one CBT ($C_2B_{10}H_{11}S$) loss from the parent cluster. Further increase of the CE to 50 eV led to the appearance of another peak, at m/z 3082.75, with a 4+ charge state, due to the loss of two CBT ligands from the parent cluster. Another prominent peak that appeared at m/z 2957.93 with a 4+ charge state is assigned to the composition $[Ag_{59}S_{12}(CBT)_{29}]^{4+}$. Two other peaks of lower intensity at m/z 2913.92 and 2887.07 (at CE 50 eV) are assigned to $[Ag_{59}S_{12}(CBT)_{28}]^{4+}$ and $[Ag_{58}S_{12}(CBT)_{28}]^{4+}$, respectively. With increasing CE to 60 eV, another peak appeared at m/z 2745.44 (with 4+ charge state), assigned to $[Ag_{56}S_{12}(CBT)_{26}]^{4+}$. The specific mass losses of 849.96 correspond to $[Ag_3(CBT)_3]$ fragments, which correspond to the structural motifs observed on the surface of the cluster (as resolved through SC XRD). We did not observe any specific fragments characteristic of the losses of silver-sulfide moieties, which clearly suggested stronger binding of the interstitial sulfides. Mass spectrometry analysis of the DMF solution, after dissolving selected single crystals, also confirmed the presence of nitrate (NO_3^-) counterions in the crystal structure (see Figure S25). These counterions are hidden inside the lattice and contribute to unresolved residual electron density around the cluster in the single-crystal XRD analysis (see Figure S23).

High-resolution transmission electron microscopic (HRTEM) investigation of a selected microcrystal shows the presence of small particles uniform in size with an average diameter of 1.4 ± 0.1 nm (see Figure S26). The drop-cast cluster solution displayed a similar distribution of particles in the lower magnification TEM analysis (see Figure S27). However, at higher magnifications with increased beam exposure, we observed beam-induced aggregation and a corresponding size expansion. The original size of ∼1.4 nm matches the molecular dimensions of the metal-sulfide skeleton of the cluster, as measured using data from SC XRD analysis (Figure S28). Additional characterization of the cluster was performed using X-ray photoelectron spectroscopy (XPS) and infrared spectroscopy. The XPS survey scan of freshly prepared microcrystals confirms the presence of Ag (368.2 and 374.1 eV), S (161.3 and 162.9 eV), B (189.8 eV), and C (285.0 eV) elements, corresponding to their character-

https://doi.org/10.1021/acsnano.5c11836
ACS Nano XXXX, XXX, XXX−XXX

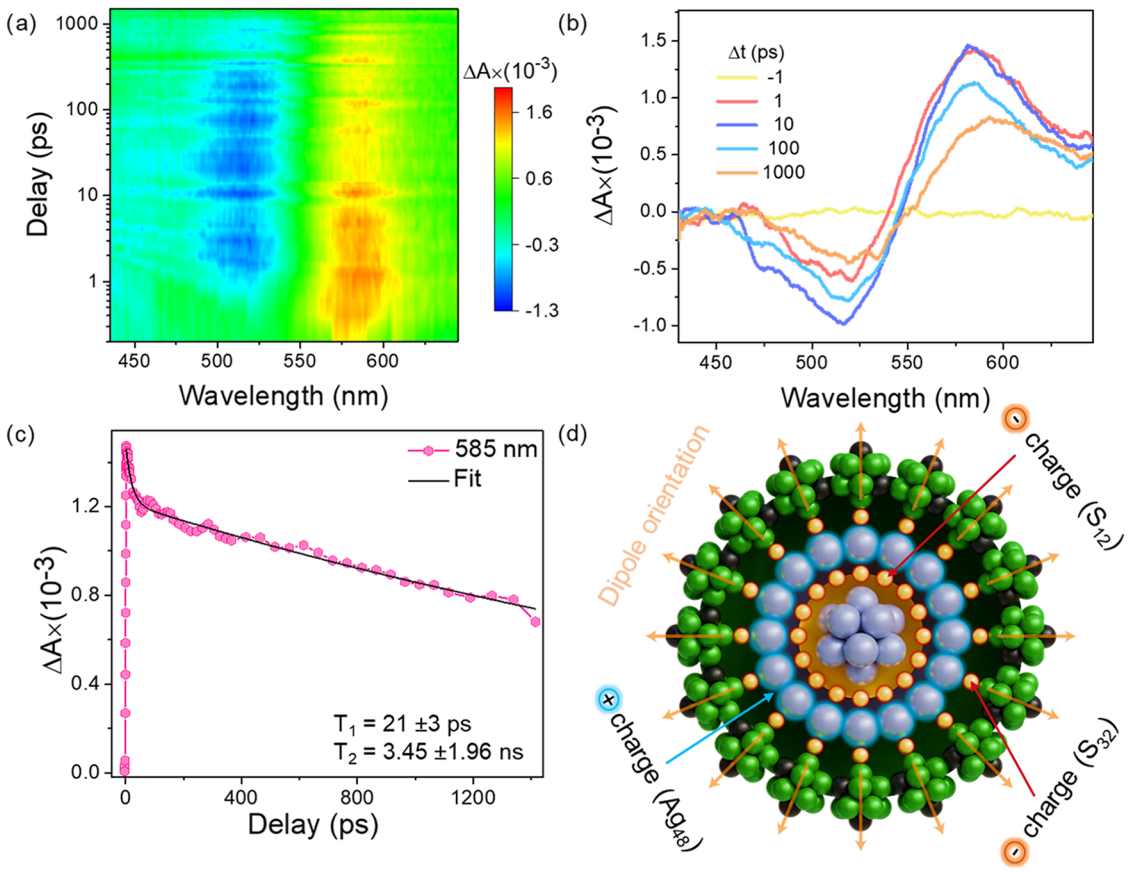

Figure 4. (a) Pseudo color map of femtosecond-TA for the Ag_{62} cluster in DMF solution by a pump excitation of 400 nm and fluence of 200 $\mu J \cdot cm^{-2}$. (b) Selected TA spectral profile as a function of time delay. (c) Kinetic decay traces for a 585 nm ESA signal. (d) A schematic representation of the multilayer charge separation within the cluster.

istic features (see Figure S29). The binding energy (BE) values of Ag $3d_{5/2}$ and $3d_{3/2}$ are consistent with those of the mixed metallic Ag(0) and Ag(1+) oxidation states. A detailed spectral scan of the S 2p region revealed two types of sulfur (1:3 ratio) in the cluster: inner sulfide with binding energies at 161.63 and 162.81 eV for S $2p_{3/2}$ and $2p_{1/2}$, and thiolate sulfide (from CBT) with binding energies at 162.99 and 164.17 eV for S $2p_{3/2}$ and $2p_{1/2}$, respectively (see Figure S30). Additionally, two peaks were observed at 401.5 eV (N 1s) and 531.9 eV (O 1s), corresponding to nitrogen and oxygen, respectively, originating from nitrate counterions in the crystal (Figure S29). Infrared (IR) spectroscopy further confirmed changes in the ligand shell associated with the decarboxylation of the starting ligand, M_9-COOH, during the solvothermal reaction. The IR spectrum of the Ag_{62} cluster exhibits characteristic bands at 2602 and 3042 cm^{-1}, corresponding to B−H and C−H stretching vibrations, similar to those observed in the spectra of M_9 or M_9-COOH molecules (see Figure S31). Additionally, carborane cage breathing and B−B bending vibrational modes were detected at 860 and 724 cm^{-1}, respectively. Weakly resolved, low-intensity bands associated with B−B and B−C bending vibrations were observed, likely due to the presence of electron-dense silver atoms near the carborane in the cluster. An important feature is the absence of C−O (1287 cm^{-1}), O−H (1417 cm^{-1}), and C═O (1713 cm^{-1}) bands, which are characteristic of M_9-COOH. Their absence in the spectrum of the Ag_{62} cluster clearly confirms the decarboxylation process during solvothermal synthesis. In conjunction with other methods, IR characterization confirms the presence of decarboxylated *meta*-carborane-thiolate as a surface envelope of the metal cluster. Metal-catalyzed thermal decarboxylation of carborane acids has been reported in previous studies.[69,70] The presence of the 1383 cm^{-1} vibrational band (antisymmetric N−O stretching band) further confirms the nitrate as counterions in the crystals. So, the composition of the compound is $[Ag_{62}S_{12}(CBT)_{32}](NO_3)_4$.

Optical Properties. The optical absorption spectrum of the Ag_{62} nanocluster (measured in DMF solution) exhibits one prominent absorption band centered at 530 nm (2.34 eV) along with two shoulder bands at 446 nm (2.78 eV) and 400 nm (3.1 eV) (Figure 3b). The characteristic optical absorption bands representing molecule-like discrete electronic energy levels suggest a transition from a molecular regime to a bulk metallic regime. UV−visible absorption spectra recorded at specific intervals over a period of half a year, using the same solution, showed no spectral changes, indicating remarkable stability of the nanocluster (see Figure S32), especially in comparison to a cluster of similar nuclearity protected by conventional organothiolate (*i.e.*, 2,4-dimethylbenzenethiolate) ligands.[71]

Ultrafast femtosecond transient absorption (fs-TA) studies were performed to understand the excited-state dynamics of the Ag_{62} nanocluster. In the measurement, the Ag_{62} nanocluster was excited using 120 fs pump pulses centered at 400 nm (3.1 eV). The resulting excited-state dynamics were investigated using time-delayed probe pulses. The color plot of obtained TA and spectral cross sections at selected time-delays with pump fluence of 200 $\mu J/cm^2$ is plotted in Figure 4a,b.

https://doi.org/10.1021/acsnano.5c11836
ACS Nano XXXX, XXX, XXX−XXX

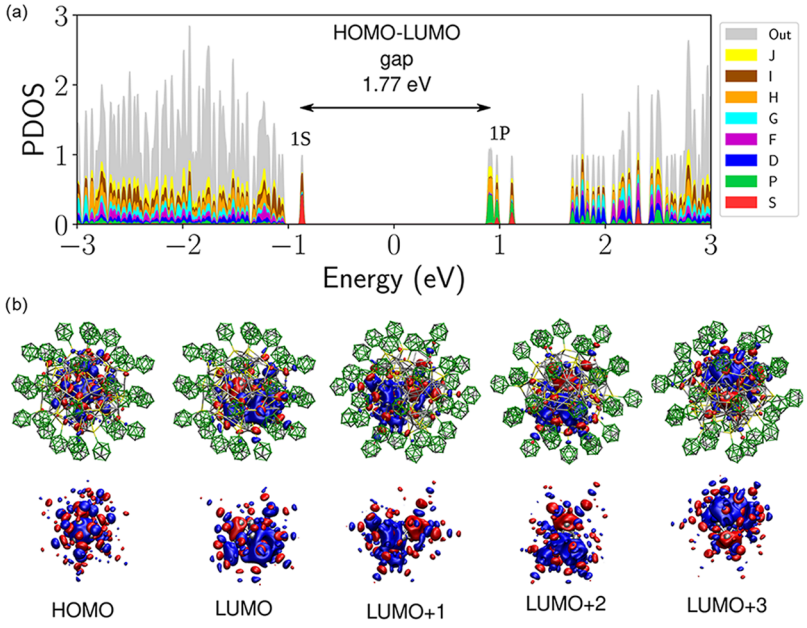

Figure 5. (a) Projected density of electron states to spherical harmonics functions centered at the center of the mass of the cluster. (b) The frontier molecular orbitals visualized with and without the full atomic structure from HOMO to LUMO+3 states.

From these figures, we see that the main TA features are ground state photobleaching (GSPB) in the regime of 515 nm, and excited state absorption (ESA) starts from 550 nm. The GSPB is located in the regime, where we observed a primary optical absorption band centered at 530 nm (see Figure 3b), and it represents the filling of closely spaced electronic excited states by the pump excitation. Further, the ESA arises from the transition of initially photoexcited states to higher excited states. We also see that ESA grows quickly while GSPB grows relatively slowly in the TA map (Figure 4a). To get more insight into these features for a longer time scale, we have plotted the time evolution profiles of TA for both GSPB and ESA in Figures S33 and 4c. These figures reveal a fast decay of excited states with a lifetime of 760 ± 23 ps for 515 nm GSPB. In contrast, the 585 nm ESA band exhibited a fast component with a lifetime of 21 ± 3 ps and stable excited states with a lifetime of 3.45 ± 1.96 ns. We also investigated the TA features at different pump fluences of 100 and 200 $\mu J \cdot cm^{-2}$ (shown in Figure S34). From this comparison, we see a small increase (ΔA of 0.2×10^{-3}) for the GSPB signal and a relatively large increase (ΔA of 0.6×10^{-3}) for the ESA signal upon increasing the pump fluence from 100 to 200 $\mu J \cdot cm^{-2}$.

The decay time of the excited states remains unaffected by the pump fluence of 100 $\mu J \cdot cm^{-2}$ (as shown in Figure S35). This result of invariant lifetime is as per the molecular nature of Ag_{62}, where relaxation of the excited states does not change as a function of the pump fluence.[72] An insight into such distinct behavior indicates multilayer charge separation within the molecule. A comprehensive analysis of the cluster indicates that the silver-sulfide structure, specifically $Ag_{62}S_{12}S_{32}$, has a charge state of 4+ as observed from the mass spectrometry analysis depicted in Figure 3a. Considering the electronegativity difference between silver and sulfur, along with the strong metallic bonding in the inner Ag_{14} core, the structure of $[Ag_{62}S_{12}S_{32}]^{4+}$ can be understood as comprising four distinct layers. At the center is a charge-neutral Ag_{14} core, surrounded by a S_{12} ring that carries −12 charges. Outside of this, there is a positively charged Ag_{48} layer with +48 charges, followed by an outer S_{32} layer that has −32 charges, as schematically illustrated in Figure 4d. This core−shell architecture of the cluster suggests a distinct photophysical mechanism for excited-state dynamics after pump excitation. Initially, photoexcitation creates excited states dominantly localized on the outer S_{32} shell. This immediate population of shells causes the prompt rise of the ESA signal. Subsequently, these electrons move from the outer shell toward the inner Ag_{14} core in an interlayer charge transfer event. This charge transfer process is experimentally observed in the form of a time-delayed appearance of the GSPB signal. Finally, these electrons dispersed on the core and shell relax back to the ground state through two different pathways with distinct time scales of ∼760 ps and 3.45 ns. Excited-state dynamics influenced by the electronic perturbation from secondary metal atom dopants was also observed in gold nanoclusters.[73] Further, our suggested mechanism is supported by computational investigation of the Ag_{62} cluster that reveals that the absorption peak around 530 nm arises from the core part of the cluster (see below). As a result, the electron mobility of excited states within this charged multilayer can give rise to stable ESA and GSPB features in the cluster.

The Ag_{62} cluster did not exhibit any strong visible luminescence in either solution or in the solid state when exposed to 365 nm UV light (see inset of Figure S36). PL excitation measurement showed two excitation bands centered at 505 nm (2.45 eV) and 433 nm (2.86 eV) for the cluster, which are close to the absorption bands of the cluster (see Figure S36a). The cluster showed a weak NIR emission band centered at around 988 nm (1.25 eV) upon photoexcitation by 500 nm (2.48 eV) (shown in Figure S36b). Intermetallic charge transfer across charged multilayers rather than metal to ligand (ML) or ligand to metal (LM) charge transfer may contribute to the observed weak NIR emission, distinguishing it from the red-emitting Ag_{62} clusters encapsulated by *tert*-butyl thiolate ligands.[74,75]

Computational Insights. Computational modeling of the Ag_{62} nanocluster was performed with density functional theory

https://doi.org/10.1021/acsnano.5c11836
ACS Nano XXXX, XXX, XXX−XXX

(DFT) using GPAW (see details of methods in the Supporting Information file). The initial structure, as obtained from the single-crystal X-ray diffraction analysis, was optimized using a real-space grid and Perdew–Burke–Ernzerhof functional, after which further analysis of electronic and optical properties was done using the GLLB-SC functional. At first, the electron states were projected with respect to spherical harmonic functions centered at the center of the mass of the cluster. This analysis reveals the superatom state symmetries that are delocalized in the inner metal core of the cluster.[76]

It is noted that the $[Ag_{62}S_{12}(CBT)_{32}]^{4+}$ cluster has a valence electron count of 2. This is calculated using the formula ($Nv_A - M - Z$), where Nv_A represents the total valence electrons of the metal atoms, M is the total electrons of electron-withdrawing ligands, and Z denotes the charge of the cluster.[76] In this case, the calculation is as follows: $[62 - (12 \times 2) - 32 - 4 = 2]$. The DFT results in Figure 5a show a clear change from 1S symmetric states to 1P nonsymmetric states when going over the HOMO–LUMO gap (1.77 eV), which indicates that the system could be characterized as a two-electron superatom system. These delocalized superatom states are present mostly on the inner $Ag_{14}S_{12}$ part (as is visualized in Figure 5b), which indicates this part as the two-electron superatom "nucleus". The visualized 1P states are non-symmetric with respect to the center of the cluster and reflect the underlying symmetry of the inner $Ag_{14}S_{12}$ part (the S_{12} shell has an icosahedral symmetry).

Next, we calculated the optical absorption spectrum using the linear response time-dependent density functional theory (Figure 6). The estimated optical gap of ~700 nm is rather

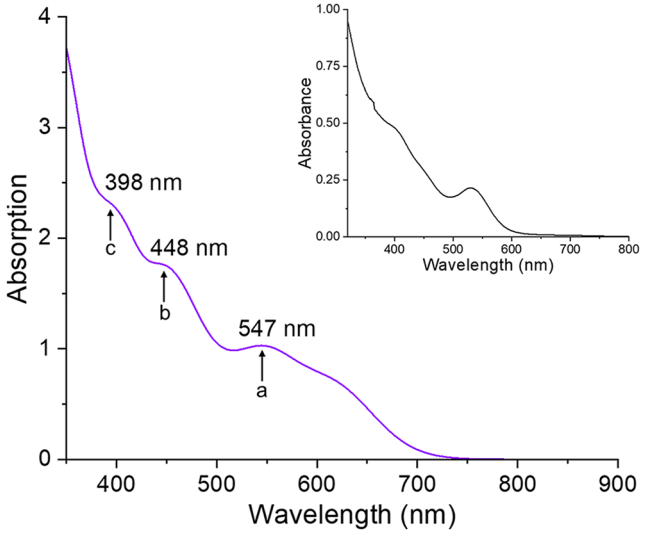

Figure 6. Calculated optical absorption spectrum of the Ag_{62} cluster (in purple) as compared to the experimental spectrum shown in the inset. The main features are labeled with arrows.

close to the measured gap of ~630 nm. The absorption spectrum has three main features in very good agreement with the experimental results. The overall shape of the calculated spectrum and the positions of the main features at 547, 448, and 398 nm coincide well with the measured spectrum. The two shortest wavelength bands (398 and 448 nm) are almost precisely at the same positions as the measured peaks (400 and 446 nm, respectively). The 547 nm peak has a shoulder around 617 nm, while the measured peak at 530 nm has a single maximum.

Origin of the absorption bands was analyzed using time-dependent density functional perturbation theory and dipole transition contribution maps (DTCM). The DTCM shows the most important strengthening and screening contributions in a contour plot for each band as decomposed to the transitions between occupied and unoccupied Kohn–Sham states. The analysis was done here for all three main bands and the longest wavelength shoulder. All of the DTCM plots are shown in Figure S37. Analysis of the shoulder feature at 617 nm in Figure S37a confirms the optical activity of the 1S to 1P transitions over the HOMO–LUMO gap. The first main peak still has a weak contribution from 1S to 1P transitions, but the main contribution is already from the states between −1.0 eV and −1.5 eV to 1P states. Based on the analysis, there is no optical activity from the 1S to LUMO+3 state, which can therefore be separated from the 1P states seen at LUMO, LUMO+1, and LUMO+2. For the two shorter wavelength peaks (547 and 448 nm), the main contributions are from lower energy occupied states between −1.0 eV and −2.0 eV to 1P states, while the shortest wavelength peak (398 nm) does not have contributions from 1S or 1P states.

CONCLUSIONS

In summary, we have synthesized a large silver/silver-sulfide nanocluster of composition $[Ag_{62}S_{12}(CBT)_{32}]^{4+}$. This nanocluster, protected by *meta*-carborane-thiolates (CBTs), was prepared by a solvothermal process, starting from the metal precursor, $AgNO_3$, and ligand, M_9-COOH (where M_9-COOH is *meta*-carborane-9-thiol-12-carboxylic acid), which undergoes thermochemical decarboxylation. Structural anatomy reveals that this highly symmetrical nanocluster has an interesting multilayer structural arrangement, starting with a fcc Ag_{14} inner kernel, encapsulated by 12 sulfide atoms, followed by a layer of $[Ag_{48}(CBT)_{32}]$ shell. Symmetry analysis of the nanocluster shows that there are five layers of silver atoms, beginning from the center of the molecule: octahedron, cube, icosahedron, truncated cube, and distorted icosahedron; containing 6, 8, 12, 24, and 12 Ag atoms, respectively. The sulfur atoms form three layers: an icosahedron, a dodecahedron, and another icosahedron, consisting of 12, 20, and 12 sulfur atoms, respectively. The overall structural organization (composed of a mixture of Platonic and Archimedean solids) can be considered as a cluster-over-cluster structure, with a silver/silver-sulfide kernel encapsulated by three-dimensional carborane ligands. This is the largest metal nanocluster reported to date, modified with carborane ligands. This cluster exhibits a characteristic optical absorption feature with multiple optical absorption bands. The cluster emits weakly in the NIR region and the excited electrons move across the charged multilayer silver-sulfide skeleton of the cluster. DFT calculations show that the cluster is a two-electron superatomic system having a band gap of 1.77 eV with the lowest-energy optical transitions of 1S to 1P superatomic character. This finding showed the way for further structure–property investigations of large metal clusters decorated with various types of molecular cluster cages.

EXPERIMENTAL SECTION

Chemicals Used. Silver nitrate ($AgNO_3$) was purchased from Rankem Chemicals. *Meta*-carborane-9-thiol-12-carboxylic acid (M_9-COOH) was synthesized following our previous report.[63] Crystalline

https://doi.org/10.1021/acsnano.5c11836
ACS Nano XXXX, XXX, XXX–XXX

M_9-COOH ligands (98.9% purity) were used for the thermochemical synthesis of the Ag_{62} cluster. High-performance liquid chromatography (HPLC)-grade solvents, including dichloromethane, chloroform, *N*,*N*-dimethylformamide, acetonitrile, and methanol (99.5%), were sourced from Rankem Chemicals and Finar, India. All of the chemicals were commercially available and used as such without further purification.

Synthesis of M_9-COOH Ligand. 2 g of portion (11.33 mmol) of *meta*-carborane-9-thiol was dissolved in 100 mL of dry and freshly distilled diethyl ether under inert conditions of argon, and the flask with the reaction mixture was cooled to −78 °C using an acetone bath with dry ice. *n*-Butyllithium (10.0 mL, 24.6 mmol) was added dropwise via a septum over a period of 20 min, which resulted in a precipitate of a white solid. The mixture was further stirred for another hour before an excess of dry ice was added to it, and the mixture was then left at room temperature to warm up slowly under an argon atmosphere. Distilled water (200 mL) was added, the mixture was shaken, and the ether fraction was separated. The aqueous solution was acidified with 30 mL of aqueous solution of hydrochloric acid (∼15%), and a white solid precipitated immediately. The mixture was extracted using diethyl ether (5 × 50 mL), and the collected ether fractions were dried by standing over anhydrous $MgSO_4$. The crude product was purified by sublimation (80 °C) to yield (∼40%) the white microcrystalline product, which was used further for the synthesis of the Ag_{62} nanocluster.

Thermochemical Synthesis of the Ag_{62} Nanocluster. The Ag_{62} cluster was synthesized by following a solvothermal synthetic method. In brief, 20 mg (0.12 mM) of $AgNO_3$ was dissolved in 2 mL of methanol upon stirring. After 20 min, 3 mL of DMF was mixed with the solution, followed by a dropwise addition of 25 mg (0.11 mM) of M_9-COOH ligand (dissolved in 1 mL of DMF). After 1 h of additional stirring at room temperature, the transparent mixture was then transferred either to a closed glass bottle or a Teflon-lined hydrothermal bomb and placed in a preheated oven (75 ± 3 °C) for 15 h. A red-colored solution was formed in the container during the thermal process. After the treatment, the solution was gradually cooled to room temperature (25 °C). The red solution was centrifuged and left to crystallize at room temperature in a dark environment. Red crystals were formed at room temperature after one month of crystallization from a DMF/methanol (1:1 v/v) saturated solution. The yield of the Ag_{62} crystals was ∼75% based on $AgNO_3$. The crystalline samples were redissolved in DMF for further analysis.

ASSOCIATED CONTENT

Supporting Information

The Supporting Information is available free of charge at https://pubs.acs.org/doi/10.1021/acsnano.5c11836.

Experimental section, instrumentation, computational details, X-ray crystallographic details, and additional experimental and computational results (PDF)

M40 new file (PDF)

M50 new file (PDF)

Accession Codes

Single-crystal X-ray diffraction data of Ag_{62} (CCDC 2374547). This data can be obtained free of charge via www.ccdc.cam.ac.uk/ data_request/cif.

AUTHOR INFORMATION

Corresponding Authors

Kumaran Nair Valsala Devi Adarsh − *Department of Physics, Indian Institute of Science Education and Research Bhopal, Bhopal 462066, India;* orcid.org/0000-0002-6337-6545; Email: adarsh@iiserb.ac.in

Hannu Häkkinen − *Departments of Physics and Chemistry, Nanoscience Center, University of Jyväskylä, FI 40014 Jyväskylä, Finland;* orcid.org/0000-0002-8558-5436; Email: hannu.j.hakkinen@jyu.fi

Tomas Base − *Department of Syntheses, Institute of Inorganic Chemistry, The Czech Academy of Sciences, 250 68 Husinec-Řež, Czech Republic;* orcid.org/0000-0003-2533-8705; Email: tbase@iic.cas.cz

Thalappil Pradeep − *DST Unit of Nanoscience (DST UNS) and Thematic Unit of Excellence (TUE), Department of Chemistry, Indian Institute of Technology, Madras, Chennai 600036, India;* orcid.org/0000-0003-3174-534X; Email: pradeep@iitm.ac.in

Authors

Arijit Jana − *DST Unit of Nanoscience (DST UNS) and Thematic Unit of Excellence (TUE), Department of Chemistry, Indian Institute of Technology, Madras, Chennai 600036, India;* orcid.org/0000-0002-5676-0688

Vivek Yadav − *DST Unit of Nanoscience (DST UNS) and Thematic Unit of Excellence (TUE), Department of Chemistry, Indian Institute of Technology, Madras, Chennai 600036, India;* orcid.org/0009-0004-0244-0541

Monika Kučeráková − *Department of Structure Analysis, Institute of Physics, The Czech Academy of Sciences, Prague 8 182 21, Czech Republic;* orcid.org/0000-0002-1177-9238

Sami Malola − *Departments of Physics and Chemistry, Nanoscience Center, University of Jyväskylä, FI 40014 Jyväskylä, Finland*

Amoghavarsha Ramachandra Kini − *DST Unit of Nanoscience (DST UNS) and Thematic Unit of Excellence (TUE), Department of Chemistry, Indian Institute of Technology, Madras, Chennai 600036, India;* orcid.org/0009-0003-6863-7729

Swetashree Acharya − *DST Unit of Nanoscience (DST UNS) and Thematic Unit of Excellence (TUE), Department of Chemistry, Indian Institute of Technology, Madras, Chennai 600036, India*

Ajay K. Poonia − *Department of Physics, Indian Institute of Science Education and Research Bhopal, Bhopal 462066, India*

Jan Macháček − *Department of Syntheses, Institute of Inorganic Chemistry, The Czech Academy of Sciences, 250 68 Husinec-Řež, Czech Republic;* orcid.org/0000-0003-4723-0789

Complete contact information is available at: https://pubs.acs.org/10.1021/acsnano.5c11836

Notes

The authors declare no competing financial interest.

ACKNOWLEDGMENTS

A.J. acknowledges an institute research fellowship from IIT Madras. V.Y. and S.A. acknowledge Prime Minister's Research Fellowships (PMRF) from the Government of India (GoI). A.R.K. thanks the GoI for a CSIR fellowship. K.N.V.D.A. gratefully acknowledges funding from the Science and Engineering Research Board (project no. CRG/2019/002808) and Department of Science and Technology (FIST) project for the Department of Physics, IISER Bhopal (PSI-195/2014) and DST/NM/TUE/QM-8/2019(G)/1). T.B. and J.M. thank the support of the Ministry of Education, Youth and Sports of the Czech Republic (grant no. LTAIN19152, Program Inter-Excellence, subprogram Inter-

https://doi.org/10.1021/acsnano.5c11836
ACS Nano XXXX, XXX, XXX−XXX

Action, and the project e-INFRA CZ, ID: 90254, providing computational resources), and the Czech Academy of Sciences (project Mobility Plus DAAD 25-07). The computational work at the University of Jyväskylä was supported by the grant from the Research Council of Finland. The computations were performed at the Finnish National Supercomputing Center CSC. T.P. thanks funding from the Center of Excellence (CoE) on Molecular Materials and Functions under the Institute of Eminence (IoE) scheme of IIT Madras, Science and Engineering Research Board (SERB), India, for funding through the SPR/2021/000439 research grant and a JC Bose Fellowship.

ABBREVIATIONS

CBT, *meta*-carborane-thiolate; NIR, near-infrared; DMF, dimethylformamide; M_9-COOH, *meta*-carborane-9-thiol-12-carboxylic acid; M_9, *meta*-carborane-9-thiol; EDS, energy-dispersive spectroscopy; fcc, face-centered cubic; Ih, icosahedron; Oh, octahedron; ESI, electrospray ionization; CE, collision energy; XRD, X-ray diffraction; HRTEM, high-resolution transmission electron microscope; XPS, X-ray photoelectron spectroscopy; BE, binding energy; IR, infrared; fs-TA, femtosecond transient absorption; GSPB, ground state photobleach; ESA, excited state absorption; DFT, density functional theory; HOMO, highest occupied molecular orbital; LUMO, lowest unoccupied molecular orbital; DTCM, dipole transition contribution map.

REFERENCES

(1) Jin, R.; Zeng, C.; Zhou, M.; Chen, Y. Atomically Precise Colloidal Metal Nanoclusters and Nanoparticles: Fundamentals and Opportunities. *Chem. Rev.* **2016**, *116*, 10346−10413.

(2) Chakraborty, I.; Pradeep, T. Atomically Precise Clusters of Noble Metals: Emerging Link between Atoms and Nanoparticles. *Chem. Rev.* **2017**, *117* (12), 8208−8271.

(3) Luo, X. M.; Li, Y. K.; Dong, X. Y.; Zang, S. Q. Platonic and Archimedean Solids in Discrete Metal-Containing Clusters. *Chem. Soc. Rev.* **2023**, *52* (1), 383−444.

(4) Deng, G.; Malola, S.; Yuan, P.; Liu, X.; Teo, B. K.; Häkkinen, H.; Zheng, N. Enhanced Surface Ligands Reactivity of Metal Clusters by Bulky Ligands for Controlling Optical and Chiral Properties. *Angew. Chem., Int. Ed.* **2021**, *60* (23), 12897−12903.

(5) Reato, M.; Dainese, T.; Antonello, S.; Maran, F. Electron Transfer in Films of Atomically Precise Gold Nanoclusters. *Chem. Mater.* **2021**, *33* (11), 4177−4187.

(6) Díez, I.; Pusa, M.; Kulmala, S.; Jiang, H.; Walther, A.; Goldmann, A. S.; Müller, A. H. E.; Ikkala, O.; Ras, R. H. A. Color Tunability and Electrochemiluminescence of Silver Nanoclusters. *Angew. Chem., Int. Ed.* **2009**, *48* (12), 2122−2125.

(7) Kang, X.; Zhu, M. Tailoring the Photoluminescence of Atomically Precise Nanoclusters. *Chem. Soc. Rev.* **2019**, *48* (8), 2422−2457.

(8) Feng, A.; Hou, S.; Yan, J.; Wu, Q.; Tang, Y.; Yang, Y.; Shi, J.; Xiao, Z. Y.; Lambert, C. J.; Zheng, N.; Hong, W. Conductance Growth of Single-Cluster Junctions with Increasing Sizes. *J. Am. Chem. Soc.* **2022**, *144* (34), 15680−15688.

(9) Abbas, M. A.; Kamat, P. V.; Bang, J. H. Thiolated Gold Nanoclusters for Light Energy Conversion. *ACS Energy Lett.* **2018**, *3* (4), 840−854.

(10) Luo, Z.; Zheng, K.; Xie, J. Engineering Ultrasmall Water-Soluble Gold and Silver Nanoclusters for Biomedical Applications. *Chem. Commun.* **2014**, *50* (40), 5143−5155.

(11) Jose, A.; Jana, A.; Gupte, T.; Nair, A. S.; Unni, K.; Nagar, A.; Kini, A. R.; Spoorthi, B. K.; Jana, S. K.; Pathak, B.; Pradeep, T. Vertically Aligned Nanoplates of Atomically Precise Co_6S_8 Cluster for Practical Arsenic Sensing. *ACS Mater. Lett.* **2023**, *5* (3), 893−899.

(12) Kumar, J. S.; Jana, A.; Raman, J.; Veera, H. M.; Kini, A. R.; Roy, J.; Jana, S. K.; Thomas, T.; Pradeep, T. Cysteine-Protected Antibacterial Spheroids of Atomically Precise Copper Clusters for Direct and Affordable Arsenic Detection from Drinking Water. *Environ. Sci. Technol. Lett.* **2024**, *11* (8), 831−837.

(13) Hua, Y.; Huang, J. H.; Shao, Z. H.; Luo, X. M.; Wang, Z. Y.; Liu, J. Q.; Zhao, X.; Chen, X.; Zang, S. Q. Composition-Dependent Enzyme Mimicking Activity and Radiosensitizing Effect of Bimetallic Clusters to Modulate Tumor Hypoxia for Enhanced Cancer Therapy. *Adv. Mater.* **2022**, *34*, No. 2203734.

(14) Qin, L.; Sun, F.; Gong, Z.; Ma, G.; Chen, Y.; Tang, Q.; Qiao, L.; Wang, R.; Liu, Z. Q.; Tang, Z. Electrochemical NO_3^- Reduction Catalyzed by Atomically Precise $Ag_{30}Pd_4$ Bimetallic Nanocluster: Synergistic Catalysis or Tandem Catalysis? *ACS Nano* **2023**, *17* (13), 12747−12758.

(15) Du, Y.; Sheng, H.; Astruc, D.; Zhu, M. Atomically Precise Noble Metal Nanoclusters as Efficient Catalysts: A Bridge between Structure and Properties. *Chem. Rev.* **2020**, *120* (2), 526−622.

(16) Kunwar, P.; Hassinen, J.; Bautista, G.; Ras, R. H. A.; Toivonen, J. Direct Laser Writing of Photostable Fluorescent Silver Nanoclusters in Polymer Films. *ACS Nano* **2014**, *8* (11), 11165−11171.

(17) Wang, Z.; Alkan, F.; Aikens, C. M.; Kurmoo, M.; Zhang, Z. Y.; Song, K. P.; Tung, C. H.; Sun, D. An Ultrastable 155-Nuclei Silver Nanocluster Protected by Thiacalix[4]Arene and Cyclohexanethiol for Photothermal Conversion. *Angew. Chem., Int. Ed.* **2022**, *61*, No. e202206742.

(18) Wang, Z.; Li, L.; Feng, L.; Gao, Z.; Tung, C.; Zheng, L.; Sun, D. Solvent-Controlled Condensation of $[Mo_2O_5(PTC4A)_2]^{6-}$ Metalloligand in Stepwise Assembly of Hexagonal and Rectangular Ag_{18} Nanoclusters. *Angew. Chem.* **2022**, *134* (20), No. e202200823, DOI: 10.1002/ange.202200823.

(19) Fuhr, O.; Dehnen, S.; Fenske, D. Chalcogenide Clusters of Copper and Silver from Silylated Chalcogenide Sources. *Chem. Soc. Rev.* **2013**, *42* (4), 1871−1906.

(20) Su, Y. M.; Wang, Z.; Tung, C. H.; Sun, D.; Schein, S. Keplerate Ag_{192} Cluster with 6 Silver and 14 Chalcogenide Octahedral and Tetrahedral Shells. *J. Am. Chem. Soc.* **2021**, *143* (33), 13235−13244.

(21) Langer, R.; Breitung, B.; Wünsche, L.; Fenske, D.; Fuhr, O. Functionalised Silver Chalcogenide Clusters. *Z. Anorg. Allg. Chem.* **2011**, *637* (7−8), 995−1006.

(22) Bestgen, S.; Fuhr, O.; Breitung, B.; Kiran Chakravadhanula, V. S.; Guthausen, G.; Hennrich, F.; Yu, W.; Kappes, M. M.; Roesky, P. W.; Fenske, D. $[Ag_{115}S_{34}(SCH_2C_6H_4{}^tBu)_{47}(Dpph)_6]$: Synthesis, Crystal Structure and NMR Investigations of a Soluble Silver Chalcogenide Nanocluster. *Chem. Sci.* **2017**, *8* (3), 2235−2240.

(23) Fenske, D.; Persau, C.; Dehnen, S.; Anson, C. E. Synthesen Und Kristallstrukturanalysen Der Ag-S-Cluster $[Ag_{70}S_{20}(SPh)_{28}(Dppm)_{10}](CF_3CO_2)_2$ and $[Ag_{262}S_{100}(S^tBu)_{62}(Dppb)_6]$. *Angew. Chem.* **2004**, *116* (3), 309−313.

(24) Anson, C. E.; Eichöfer, A.; Issac, I.; Fenske, D.; Fuhr, O.; Sevillano, P.; Persau, C.; Stalke, D.; Zhang, J. Synthesis and Crystal Structures of the Ligand-Stabilized Silver Chalcogenide Clusters $[Ag_{154}Se_{77}(Dppxy)_{18}]$, $[Ag_{320}(S^tBu)_{60}S_{130}(Dppp)_{12}]$, $[Ag_{352}S_{128}(S^tC_5H_{11})_{96}]$, and $[Ag_{490}S_{188}(S^tC_5H_{11})_{114}]$. *Angew. Chem., Int. Ed.* **2008**, *47* (7), 1326−1331.

(25) Zhang, S. S.; Havenridge, S.; Zhang, C.; Wang, Z.; Feng, L.; Gao, Z. Y.; Aikens, C. M.; Tung, C. H.; Sun, D. Sulfide Boosting Near-Unity Photoluminescence Quantum Yield of Silver Nanocluster. *J. Am. Chem. Soc.* **2022**, *144* (40), 18305−18314.

(26) Wu, T.; Zhang, Q.; Hou, Y.; Wang, L.; Mao, C.; Zheng, S. T.; Bu, X.; Feng, P. Monocopper Doping in Cd-In-S Supertetrahedral Nanocluster via Two-Step Strategy and Enhanced Photoelectric Response. *J. Am. Chem. Soc.* **2013**, *135* (28), 10250−10253.

(27) Song, Y.; Lambright, K.; Zhou, M.; Kirschbaum, K.; Xiang, J.; Xia, A.; Zhu, M.; Jin, R. Large-Scale Synthesis, Crystal Structure, and Optical Properties of the $Ag_{146}Br_2(SR)_{80}$ Nanocluster. *ACS Nano* **2018**, *12* (9), 9318−9325.

(28) Desireddy, A.; Conn, B. E.; Guo, J.; Yoon, B.; Barnett, R. N.; Monahan, B. M.; Kirschbaum, K.; Griffith, W. P.; Whetten, R. L.;

https://doi.org/10.1021/acsnano.5c11836
ACS Nano XXXX, XXX, XXX−XXX

Landman, U.; Bigioni, T. P. Ultrastable Silver Nanoparticles. *Nature* **2013**, *501* (7467), 399−402.
(29) Joshi, C. P.; Bootharaju, M. S.; Alhilaly, M. J.; Bakr, O. M. $[Ag_{25}(SR)_{18}]$-: The "Golden" Silver Nanoparticle. *J. Am. Chem. Soc.* **2015**, *137* (36), 11578−11581.
(30) Yang, H.; Wang, Y.; Huang, H.; Gell, L.; Lehtovaara, L.; Malola, S.; Häkkinen, H.; Zheng, N. All-Thiol-Stabilized Ag_{44} and $Au_{12}Ag_{32}$ Nanoparticles with Single-Crystal Structures. *Nat. Commun.* **2013**, *4*, No. 2422.
(31) Yang, H.; Wang, Y.; Chen, X.; Zhao, X.; Gu, L.; Huang, H.; Yan, J.; Xu, C.; Li, G.; Wu, J.; Edwards, A. J.; Dittrich, B.; Tang, Z.; Wang, D.; Lehtovaara, L.; Häkkinen, H.; Zheng, N. Plasmonic Twinned Silver Nanoparticles with Molecular Precision. *Nat. Commun.* **2016**, *7*, No. 12809.
(32) Ren, L.; Yuan, P.; Su, H.; Malola, S.; Lin, S.; Tang, Z.; Teo, B. K.; Häkkinen, H.; Zheng, L.; Zheng, N. Bulky Surface Ligands Promote Surface Reactivities of $[Ag_{141}X_{12}(S\text{-}Adm)_{40}]^{3+}$ (X = Cl, Br, I) Nanoclusters: Models for Multiple-Twinned Nanoparticles. *J. Am. Chem. Soc.* **2017**, *139* (38), 13288−13291.
(33) Zhou, Q.; Kaappa, S.; Malola, S.; Lu, H.; Guan, D.; Li, Y.; Wang, H.; Xie, Z.; Ma, Z.; Häkkinen, H.; Zheng, N.; Yang, X.; Zheng, L. Real-Space Imaging with Pattern Recognition of a Ligand-Protected Ag_{374} Nanocluster at Sub-Molecular Resolution. *Nat. Commun.* **2018**, *9*, No. 2948.
(34) Bootharaju, M. S.; Lee, S.; Deng, G.; Malola, S.; Baek, W.; Häkkinen, H.; Zheng, N.; Hyeon, T. $Ag_{44}(EBT)_{26}(TPP)_4$ Nanoclusters With Tailored Molecular and Electronic Structure. *Angew. Chem.* **2021**, *133* (16), 9120−9126.
(35) Bootharaju, M. S.; Dey, R.; Gevers, L. E.; Hedhili, M. N.; Basset, J. M.; Bakr, O. M. A New Class of Atomically Precise, Hydride-Rich Silver Nanoclusters Co-Protected by Phosphines. *J. Am. Chem. Soc.* **2016**, *138* (42), 13770−13773.
(36) Lei, Z.; Wan, X.-K.; Yuan, S.-F.; Guan, Z.-J.; Wang, Q.-M. Alkynyl Approach toward the Protection of Metal Nanoclusters. *Acc. Chem. Res.* **2018**, *51* (10), 2465−2474.
(37) Qu, M.; Li, H.; Xie, L. H.; Yan, S. T.; Li, J. R.; Wang, J. H.; Wei, C. Y.; Wu, Y. W.; Zhang, X. M. Bidentate Phosphine-Assisted Synthesis of an All-Alkynyl-Protected Ag_{74} Nanocluster. *J. Am. Chem. Soc.* **2017**, *139* (36), 12346−12349.
(38) Najafabadi, B. K.; Corrigan, J. F. N-Heterocyclic Carbene Stabilized Ag-P Nanoclusters. *Chem. Commun.* **2015**, *51* (4), 665−667.
(39) Dhayal, R. S.; Liao, J.-H.; Liu, Y.-C.; Chiang, M.-H.; Kahlal, S.; Saillard, J.-Y.; Liu, C. W. $[Ag_{21}\{S_2P(O^iPr)_2\}_{12}]^+$: An Eight-Electron Superatom. *Angew. Chem.* **2015**, *127*, 3773−3777.
(40) Yuan, S. F.; Xu, C. Q.; Liu, W. Di.; Zhang, J. X.; Li, J.; Wang, Q. M. Rod-Shaped Silver Supercluster Unveiling Strong Electron Coupling between Substituent Icosahedral Units. *J. Am. Chem. Soc.* **2021**, *143* (31), 12261−12267.
(41) Cerretani, C.; Kanazawa, H.; Vosch, T.; Kondo, J. Crystal Structure of a NIR-Emitting DNA-Stabilized Ag_{16} Nanocluster. *Angew. Chem.* **2019**, *131* (48), 17313−17317.
(42) Guan, Z. J.; Zeng, J. L.; Nan, Z. A.; Wan, X. K.; Lin, Y. M.; Wang, Q. M. Thiacalix[4]Arene: New Protection for Metal Nanoclusters. *Sci. Adv.* **2016**, *2* (8), No. e1600323.
(43) Wang, Z.; Su, H. F.; Gong, Y. W.; Qu, Q. P.; Bi, Y. F.; Tung, C. H.; Sun, D.; Zheng, L. S. A Hierarchically Assembled 88-Nuclei Silver-Thiacalix[4]Arene Nanocluster. *Nat. Commun.* **2020**, *11*, No. 308.
(44) Liu, K.-G.; Gao, X.-M.; Liu, T.; Hu, M.-L.; Jiang, D. All-Carboxylate-Protected Superatomic Silver Nanocluster with an Unprecedented Rhombohedral Ag_8 Core. *J. Am. Chem. Soc.* **2020**, *142* (40), 16905−16909.
(45) Poater, J.; Viñas, C.; Bennour, I.; Escayola, S.; Solà, M.; Teixidor, F. Too Persistent to Give Up: Aromaticity in Boron Clusters Survives Radical Structural Changes. *J. Am. Chem. Soc.* **2020**, *142* (20), 9396−9407.
(46) Núñez, R.; Tarrés, M.; Ferrer-Ugalde, A.; De Biani, F. F.; Teixidor, F. Electrochemistry and Photoluminescence of Icosahedral Carboranes, Boranes, Metallacarboranes, and Their Derivatives. *Chem. Rev.* **2016**, *116* (23), 14307−14378.
(47) Fister, T. T.; Vila, F. D.; Seidler, G. T.; Svec, L.; Linehan, J. C.; Cross, J. O. Local Electronic Structure of Dicarba-Closo-Dodecarboranes $C_2B_{10}H_{12}$. *J. Am. Chem. Soc.* **2008**, *130* (3), 925−932.
(48) Jana, A.; Jash, M.; Dar, W. A.; Roy, J.; Chakraborty, P.; Paramasivam, G.; Lebedkin, S.; Kirakci, K.; Manna, S.; Antharjanam, S.; Machacek, J.; Kucerakova, M.; Ghosh, S.; Lang, K.; Kappes, M. M.; Base, T.; Pradeep, T. Carborane-Thiol Protected Copper Nanoclusters: Stimuli-Responsive Materials with Tunable Phosphorescence. *Chem. Sci.* **2023**, *14* (6), 1613−1626.
(49) Jana, A.; Duary, S.; Das, A.; Kini, A. R.; Acharya, S.; Machacek, J.; Pathak, B.; Base, T.; Pradeep, T. Multicolor Photoluminescence of Cu_{14} Clusters Modulated Using Surface Ligands. *Chem. Sci.* **2024**, *15* (34), 13741−13752.
(50) Wang, J.; Cai, J.; Ren, K. X.; Liu, L.; Zheng, S. J.; Wang, Z. Y.; Zang, S. Q. Stepwise Structural Evolution toward Robust Carboranealkynyl-Protected Copper Nanocluster Catalysts for Nitrate Electroreduction. *Sci. Adv.* **2024**, *10* (18), No. eadn7556.
(51) Wang, J.; Xu, F.; Wang, Z.-Y.; Zang, S.-Q.; Mak, T. C. W. Ligand-Shell Engineering of a Au_{28} Nanocluster Boosts Electrocatalytic CO_2 Reduction. *Angew. Chem., Int. Ed.* **2022**, *61*, No. e202207492.
(52) Jana, A.; Spoorthi, B. K.; Nair, A. S.; Nagar, A.; Pathak, B.; Base, T.; Pradeep, T. A Luminescent Cu_4 Cluster Film Grown by Electrospray Deposition: A Nitroaromatic Vapour Sensor. *Nanoscale* **2023**, *15*, 8141−8147.
(53) Kini, A. R.; Debta, S.; Jana, A.; Aparna, C.; Yadav, V.; Kusiak, N.; Base, T.; Waghmare, U. V.; Ghosh, P.; Pradeep, T. Nanomechanical Investigations of Crystals of Copper Nanocluster Isomorphs: Enhanced Hardness of the Low-Density Analogue. *Chem. Mater.* **2025**, *37* (3), 1284−1296.
(54) Wang, Q. Y.; Wang, J.; Wang, S.; Wang, Z. Y.; Cao, M.; He, C. L.; Yang, J. Q.; Zang, S. Q.; Mak, T. C. W. O-Carborane-Based and Atomically Precise Metal Clusters as Hypergolic Materials. *J. Am. Chem. Soc.* **2020**, *142* (28), 12010−12014.
(55) Huang, J. H.; Ji, A. Q.; Wang, Z. Y.; Wang, Q. Y.; Zang, S. Q. Boosting 2000-Fold Hypergolic Ignition Rate of Carborane by Substitutes Migration in Metal Clusters. *Adv. Sci.* **2024**, *11*, No. 2401861.
(56) Wang, Z. Y.; Wang, M. Q.; Li, Y. L.; Luo, P.; Jia, T. T.; Huang, R. W.; Zang, S. Q.; Mak, T. C. W. Atomically Precise Site-Specific Tailoring and Directional Assembly of Superatomic Silver Nanoclusters. *J. Am. Chem. Soc.* **2018**, *140* (3), 1069−1076.
(57) Jana, A.; Jash, M.; Poonia, A. K.; Paramasivam, G.; Islam, M. R.; Chakraborty, P.; Antharjanam, S.; Machacek, J.; Ghosh, S.; Adarsh, K. N. V. D.; Base, T.; Pradeep, T. Light-Activated Intercluster Conversion of an Atomically Precise Silver Nanocluster. *ACS Nano* **2021**, *15* (10), 15781−15793.
(58) Li, Y. L.; Wang, Z. Y.; Ma, X. H.; Luo, P.; Du, C. X.; Zang, S. Q. Distinct Photophysical Properties in Atom-Precise Silver and Copper Nanocluster Analogues. *Nanoscale* **2019**, *11* (12), 5151−5157.
(59) Yadav, V.; Jana, A.; Acharya, S.; Malola, S.; Nagar, H.; Sharma, A.; Kini, A. R.; Antharjanam, S.; Machacek, J.; Nair, K.; Devi, V.; Base, T.; Häkkinen, H.; Pradeep, T. Site-Specific Substitution in Atomically Precise Carboranethiol-Protected Nanoclusters and Concomitant Changes in Electronic Properties. *Nat. Commun.* **2025**, *16*, No. 1197.
(60) Jana, A.; Unnikrishnan, P. M.; Poonia, A. K.; Roy, J.; Jash, M.; Paramasivam, G.; Machacek, J.; Adarsh, K. N. V. D.; Base, T.; Pradeep, T. Carboranethiol-Protected Propeller-Shaped Photoresponsive Silver Nanomolecule. *Inorg. Chem.* **2022**, *61* (23), 8593−8603.
(61) Huang, J. H.; Wang, Z. Y.; Zang, S. Q.; Mak, T. C. W. Spontaneous Resolution of Chiral Multi-Thiolate-Protected Ag_{30} Nanoclusters. *ACS Cent. Sci.* **2020**, *6* (11), 1971−1976.
(62) Huang, J. H.; Si, Y.; Dong, X. Y.; Wang, Z. Y.; Liu, L. Y.; Zang, S. Q.; Mak, T. C. W. Symmetry Breaking of Atomically Precise Fullerene-like Metal Nanoclusters. *J. Am. Chem. Soc.* **2021**, *143* (32), 12439−12444.

https://doi.org/10.1021/acsnano.5c11836
ACS Nano XXXX, XXX, XXX−XXX

(63) Goronzy, D. P.; Staněk, J.; Avery, E.; Guo, H.; Bastl, Z.; Dušek, M.; Gallup, N. M.; Gün, S.; Kučeráková, M.; Levandowski, B. J.; Macháček, J.; Šícha, V.; Thomas, J. C.; Yavuz, A.; Houk, K. N.; Danlşman, M. F.; Mete, E.; Alexandrova, A. N.; Baše, T.; Weiss, P. S. Influence of Terminal Carboxyl Groups on the Structure and Reactivity of Functionalized M-Carboranethiolate Self-Assembled Monolayers. *Chem. Mater.* **2020**, *32* (15), 6800−6809.
(64) Xie, Y. P.; Shen, Y. L.; Duan, G. X.; Han, J.; Zhang, L. P.; Lu, X. Silver Nanoclusters: Synthesis, Structures and Photoluminescence. *Mater. Chem. Front.* **2020**, *4* (8), 2205−2222.
(65) Bhattarai, B.; Zaker, Y.; Atnagulov, A.; Yoon, B.; Landman, U.; Bigioni, T. P. Chemistry and Structure of Silver Molecular Nanoparticles. *Acc. Chem. Res.* **2018**, *51* (12), 3104−3113.
(66) Bootharaju, M. S.; Burlakov, V. M.; Besong, T. M. D.; Joshi, C. P.; Abdulhalim, L. G.; Black, D. M.; Whetten, R. L.; Goriely, A.; Bakr, O. M. Reversible Size Control of Silver Nanoclusters via Ligand-Exchange. *Chem. Mater.* **2015**, *27* (12), 4289−4297.
(67) White, K. E.; Avery, E. M.; Cummings, E.; Hong, Z.; Langecker, J.; Vetushka, A.; Dušek, M.; Macháček, J.; Višnák, J.; Endres, J.; Bastl, Z.; Mete, E.; Alexandrova, A. N.; Baše, T.; Weiss, P. S. Competing Intermolecular and Molecule-Surface Interactions: Dipole-Dipole-Driven Patterns in Mixed Carborane Self-Assembled Monolayers. *Chem. Mater.* **2024**, *36* (4), 2085−2095.
(68) Baše, T.; Macháček, J.; Hájková, Z.; Langecker, J.; Kennedy, J. D.; Carr, M. J. Thermal Isomerizations of Monothiolated Carboranes $(HS)C_2B_{10}H_{11}$ and the Solid-State Investigation of 9-(HS)-1,2-$C_2B_{10}H_{11}$ and 9-(HS)-1,7-$C_2B_{10}H_{11}$. *J. Organomet. Chem.* **2015**, *798*, 132−140.
(69) Lee, K.; Harper, J. L.; Kim, T. H.; Chan Noh, H.; Kim, D.; Cheong, P. H.-Y.; Lee, P. H. Regiodivergent Metal-Catalyzed B(4)- and C(1)-Selenylation of o-Carboranes. *Chem. Sci.* **2023**, *14* (3), 643−649.
(70) Quan, Y.; Xie, Z. Controlled Functionalization of o-Carborane via Transition Metal Catalyzed B-H Activation. *Chem. Soc. Rev.* **2019**, *48*, 3660−3673.
(71) Alhilaly, M. J.; Bootharaju, M. S.; Joshi, C. P.; Besong, T. M.; Emwas, A. H.; Juarez-Mosqueda, R.; Kaappa, S.; Malola, S.; Adil, K.; Shkurenko, A.; Häkkinen, H.; Eddaoudi, M.; Bakr, O. M. $[Ag_{67}(SPhMe_2)_{32}(PPh_3)_8]^{3+}$: Synthesis, Total Structure, and Optical Properties of a Large Box-Shaped Silver Nanocluster. *J. Am. Chem. Soc.* **2016**, *138* (44), 14727−14732.
(72) Wang, J. Q.; Shi, S.; He, R. L.; Yuan, S. F.; Yang, G. Y.; Liang, G. J.; Wang, Q. M. Total Structure Determination of the Largest Alkynyl-Protected Fcc Gold Nanocluster Au_{110} and the Study on Its Ultrafast Excited-State Dynamics. *J. Am. Chem. Soc.* **2020**, *142* (42), 18086−18092.
(73) Wang, X.; Zhong, Y.; Li, T.; Wang, K.; Dong, W.; Lu, M.; Zhang, Y.; Wu, Z.; Tang, A.; Bai, X. Sequential Addition of Cations Increases Photoluminescence Quantum Yield of Metal Nanoclusters near Unity. *Nat. Commun.* **2025**, *16*, No. 587.
(74) Li, G.; Lei, Z.; Wang, Q. Luminescent Molecular Ag-S Nanocluster $[Ag_{62}S_{13}(S^tBu)_{32}](BF_4)_4$. *J. Am. Chem. Soc.* **2010**, *132*, 17678−17679.
(75) Jin, S.; Wang, S.; Song, Y.; Zhou, M.; Zhong, J.; Zhang, J.; Xia, A.; Pei, Y.; Chen, M.; Li, P.; Zhu, M. Crystal Structure and Optical Properties of the $[Ag_{62}S_{12}(S^tBu)_{32}]^{2+}$ Nanocluster with a Complete Face-Centered Cubic Kernel. *J. Am. Chem. Soc.* **2014**, *136*, 15559−15565.
(76) Walter, M.; Akola, J.; Lopez-Acevedo, O.; Jadzinsky, P. D.; Calero, G.; Ackerson, C. J.; Whetten, R. L.; Grönbeck, H.; Häkkinen, H. A Unified View of Ligand-Protected Gold Clusters as Superatom Complexes. *Proc. Natl. Acad. Sci. U.S.A.* **2008**, *105* (27), 9157−9162.

https://doi.org/10.1021/acsnano.5c11836
ACS Nano XXXX, XXX, XXX−XXX